Grating-coupled surface plasmon polaritons and waveguide modes in a silver–dielectric–silver structure

Zhuo Chen, Ian R. Hooper, and J. Roy Sambles*

School of Physics, Thin Film Photonics Group, University of Exeter, Exeter EX4 4QL, UK
**Corresponding author: J.R.Sambles@exeter.ac.uk*

Received June 18, 2007; revised September 18, 2007; accepted September 21, 2007;
posted September 24, 2007 (Doc. ID 84213); published October 19, 2007

A silver–dielectric–silver structure that supports both waveguide modes and surface plasmon polaritons is explored. The upper interface between the dielectric and the silver is periodically corrugated to allow coupling of visible photons to both types of mode. Such a metallic microcavity leads to plasmonic and waveguide self-interacting bandgaps at Brillouin zone boundaries. In addition there are found other bandgaps from mode crossings within the Brillouin zone. This results specifically in a very flat photonic band due to anticrossings between a surface plasmon polariton and waveguide modes. Characterization of the observed modes in terms of their resonant electromagnetic fields is achieved by using a multilayer, multishape differential grating theory.

OCIS codes: 240.6680, 050.2770.

1. INTRODUCTION

Because microcavities may provide resonant enhancement of electromagnetic fields in optoelectronic devices, microcavities comprising a pair of highly reflecting mirrors separated by a dielectric film have been widely studied and used in a number of applications, such as light-emitting diodes [1–3], photodetectors [4,5], modulators [6], filters [7], and amplifiers [8]. The mirrors used in such structures may be either dielectric stacks or more simply metal layers. For the case of metal mirrors, surface plasmon polaritons (SPPs), which are fundamental electromagnetic excitations at the interface between a metal and a dielectric [9], may be supported as well as waveguide modes [10] if the dielectric is thick enough. On a flat metal surface the localized SPP mode cannot be directly excited by incident photons because the wave vector of the SPP mode for any given frequency is greater than that of a photon-polariton of the same frequency in the adjacent dielectric, i.e., it is nonradiative. To optically excite the SPP mode, the in-plane momentum of incident photons must be suitably increased. Lupton *et al.* [11] have shown that a microcavity with periodic texture can be used to provide an increase in light-emitting efficiency by allowing some of the energy that would be lost in a planar microcavity device to be recovered as useful radiation. In addition to an efficiency increase, structures possessing wavelength-scale texture produce photonic bandgaps [12–14]. Such photonic bandgaps may play an important role in controlling spontaneous emission and, combining them with waveguide structures, can lead to an increase in such control by placing the photonic band edge at the emission wavelength [15–18]. The design and fabrication of metallic nanostructures combining surface wave properties with microcavity resonant behavior opens up substantial new device potential.

In this study, we investigate the visible electromagnetic (EM) response of a silver-photoresist-silver layered microcavity structure in which the upper interface between the photoresist and the silver is periodically corrugated. By recording the visible reflection spectra and mapping the experimental data to a plot of reflectivity as a function of frequency and in-plane wave vector, the SPP and waveguide band structure are elaborated. In particular, the presence of a flatband caused by the anticrossings between the SPP mode and waveguide modes is confirmed experimentally. This flatband resonant frequency may be tuned by varying the amplitude of the corrugation. To fully understand the character of all the modes uncovered, the optical field distribution at the resonant frequency for each of the modes is explored.

2. EXPERIMENTS AND DISCUSSION

In Fig. 1 a schematic view of the structure and associated coordinate system under study is shown. Note that in our experiments to acquire the correct different azimuth angles (φ) the sample is rotated, not the prism. To fabricate the sample a thin silver film (acting as the entrance optical tunnel barrier and a reasonable cavity mirror), having a thickness of ~57 nm, was deposited by vacuum evaporation onto a flat silica substrate. The silver thickness chosen is such as to provide significant reflectivity while being thin enough to ensure that there is suitable strength of tunneling of the evanescent optical field. Onto this silver substrate is spin-coated a layer of Shipley SPR700 photoresist to give a waveguide layer of approximately 350 nm thickness. For such a thickness the lowest two-order waveguide modes should be accessible in the visible range. The sample is then baked at 90°C for 30 min to remove the remaining solvent from the resist

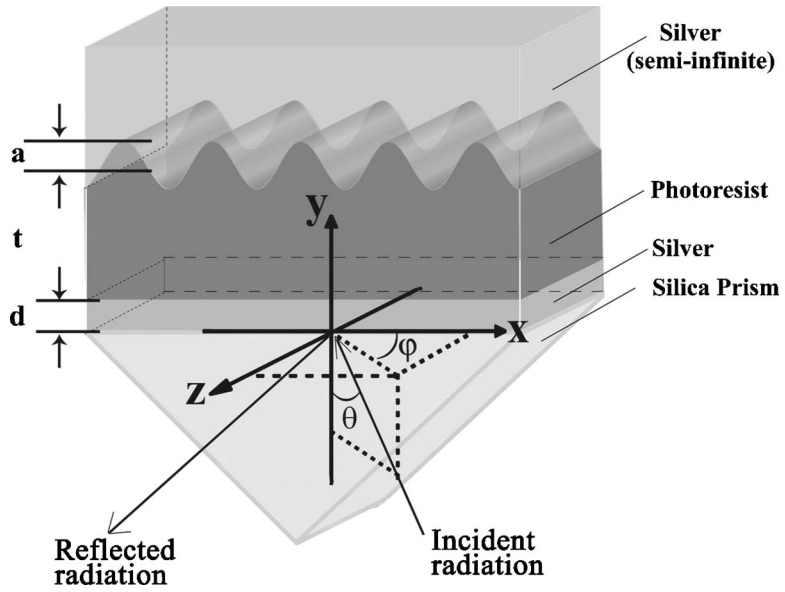

Fig. 1. Schematic illustrating the sample, the coordinate system, and the experimental geometry used in this paper. Here a is the grating amplitude, d is the thickness of the silver tunnel barrier, θ is the polar angle, φ is the azimuthal angle, and t is the average thickness of the photoresist layer. The silica substrate is optically attached to the silica prism with matching fluid. Note that in our experiments to acquire the correct different azimuth angles (φ) the sample is rotated, not the prism.

layer. Next the resist is exposed to an interference pattern, using a He–Cd laser operating at a wavelength of 325 nm, and developed in NaOH solution. The pitch, λ_g, of the grating is set at 252 nm. Post-treatment of the resist by thermal baking at 90 °C for 30 min and overnight exposure to incoherent UV ensure that the resist is fully stabilized. On top of this now-corrugated layer is deposited an optically thick (approximately 200 nm) layer of silver by thermal evaporation. Finally the microcavity sample on its silica substrate is optically attached to a 45° silica prism using matching fluid to avoid unwanted reflections from the substrate/air interface. The layered structure is described by

$$y_1(x) = d + t, \quad y_2(x) = t, \quad y_3(x) = a_0 \sin(k_g x + \phi_0) + \cdots + a_N \sin((N+1)k_g x + \phi_N) + \cdots,$$

where $y_1(x)$, $y_2(x)$, and $y_3(x)$ are the profiles of silica/thin

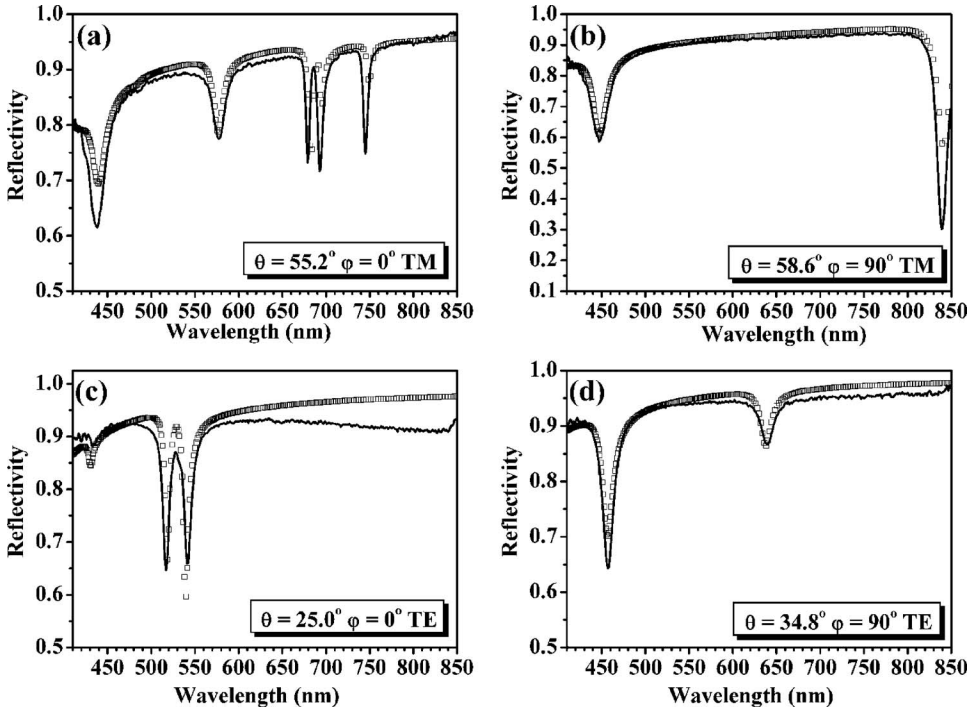

Fig. 2. Results of the wavelength-dependent reflectivity for TM polarization at angles (a) θ=55.2°, φ=0°, and (b) θ=58.6°, φ=90°, and for TE polarization at angles (c) θ=25.0°, φ=0°, and (b) θ=34.8°, φ=90°. The solid curves on each of the graphs correspond to the experimental data. The black open squares are theoretically modeled results.

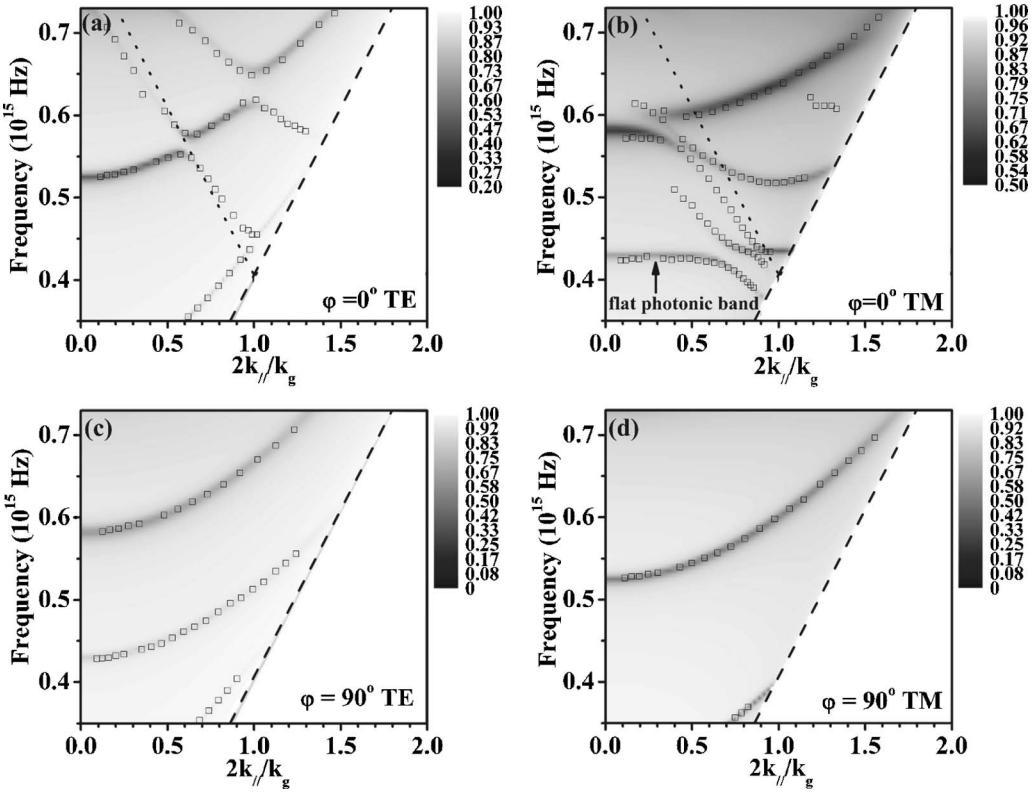

Fig. 3. Theoretical TE reflectivity for (a) $\varphi=0°$ and (c) $\varphi=90°$, and TM reflectivity for (b) $\varphi=0°$ and (d) $\varphi=90°$ as a function of frequency and in-plane wave vector. The open black squares are the mapped reflection dips that are taken from the experimental reflectivity spectra. The dashed line indicates the silica light line. The dotted line in the upper two diagrams represents the first-order diffracted silica light line. The white triangular region in the bottom right corner indicates the inaccessible region beyond the silica light line.

silver interface, thin silver/photoresist interface, and photoresist/thick silver interface, respectively, d is the thickness of the bottom silver layer, t is the average thickness of the photoresist layer, a_N is the amplitude of the Nth order harmonic component of the grating, and $k_g = 2\pi/\lambda_g$ (λ_g is the grating pitch) is the grating vector, which runs parallel to the x axis.

To determine the dispersion of the modes associated with the structure, absolute reflectivity spectra are recorded as scans in wavelengths ($410 \leq \lambda_0 \leq 850$ nm) at various fixed angles. The output from a white-light source was spectrally selected using a monochromator, and this light was then set to be p polarized, transverse magnetic (TM) or s polarized, transverse electric (TE) and made incident on the bottom surface of the silver tunnel barrier through the prism. A second polarizer, also set to TM or TE polarization, is placed directly in front of the detector. When the frequency and in-plane wave vector of the incident light match a mode, the reflectivity will show a resonant dip. In this way, by noting all the reflectivity dips, a dispersion diagram is acquired. Reflectivity data were acquired at two azimuth angles, $\varphi=0°$ (the grating grooves being perpendicular to the incident plane) and $\varphi=90°$ (the grating grooves are parallel to the incident plane) and at 20 different polar angles ($4.9° \leq \theta \leq 65.0°$) for both TM and TE polarization. Figure 2 illustrates typical TM and TE polarized wavelength-dependent absolute reflectivity data together with the modeling results for $\varphi=0°$ and $\varphi=90°$ at different polar angles. Modeling was achieved using a conical version of the differential formalism originally proposed by Chandezon *et al.* [19], in which a nonorthogonal curvilinear coordinate transformation is used to allow for easy matching of the electromagnetic boundary conditions at the interface. This computational approach has been shown to agree well with experimental data in previous studies [20,21]. To facilitate modeling over the visible domain the permittivity of the silver and photoresist are described by polynomials for both the real and imaginary parts of the permittivity [22]; although it is known that for the thinner silver film these bulk permittivities may not be exact, they are still suitable to yield a good fit to the data. The refractive index of the silica is for simplicity taken as fixed at $n=1.459$. The best comparison between the model and the experimental data is achieved, as shown in Figs. 2(a)–2(d), when the following fitting parameters are used: $a_0=40.3$ nm, $\phi_0=0°$, $a_1=-8.4$ nm, $\phi_1=-90°$, $a_2=-2.4$ nm, $\phi_2=0°$, $d=56.8$ nm, and $t=300.8$ nm.

Figure 3 shows the model TM and TE reflectivities as a function of frequency ($f=c/\lambda$) and in-plane wave vector ($k_\parallel$) for $\varphi=0°$ and $\varphi=90°$, respectively, with the experimental data (indicated as open squares) also being mapped onto this plot. The white triangular area in the bottom right corner of these plots indicates the inaccessible region beyond the silica light line. To identify each of the modes observed in the TM and TE dispersion curves, it is necessary to study the band structure of this metallic microcavity. Figure 4 shows the model band structure, obtained by inspection of the scattering matrix of the system, for all the modes (both TM and TE polarization) sup-

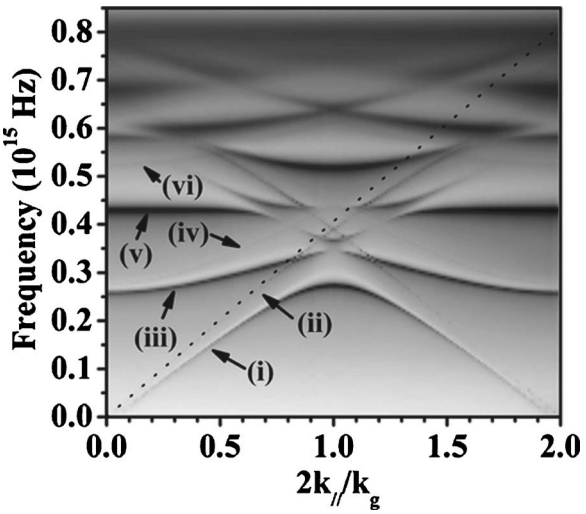

Fig. 4. Theoretical band structure for the waveguide structure at $\varphi=0°$. The unscattered modes can be identified as (i) SPP mode that is supported by silver/photoresist interface, (ii) SPP mode that propagates at the silver/silica interface, (iii) TM_1 waveguide mode, (iv) TE_1 guide mode, and (vi) TE_2 mode, respectively. Note the flat character of mode (v). The dotted line represents the light line in silica.

ported by the waveguide structure over a certain range of frequency and in-plane wave vector at $\varphi=0°$, including the evanescent modes. Modes labeled (i) and (ii) in Fig. 4 are beyond the silica light line (indicated as a dotted line) and are not accessible; these are SPP modes supported by the silver/photoresist interface and the silica/silver interface, respectively. We use the labels TM_m and TE_m to identify the various TM and TE waveguide modes, where m is an integer indicating the mth order of the guided mode. The modes (iii) and (iv) are the TM_1 and TE_1 waveguide modes, and mode (vi) is the TE_2 guided mode. Mode (v) appears flattened by the interaction of the unscattered TM_2 guided mode with both the Bragg-scattered silver/photoresist SPP mode and the Bragg-scattered TM_1 guided mode. We will discuss this flatband in more detail later in this section.

In this corrugated microcavity, due to the introduction of the periodicity, all of the modes may be "reflected" at the Brillouin zone (BZ) boundary, which causes crossings between the different branches. This gives rise to photonic bandgaps and flatband regions due to the interactions at these crossing points. Figure 3(a) shows the TE reflectivity at $\varphi=0°$. In this case, the incident optical electric field is parallel to the grating grooves, and hence no SPP modes are excited. By comparing with the band structure in Fig. 4, it is clear that only TE_1 and TE_2 guided modes can be accessed in the visible range. At the first BZ boundary $2k_{//}/k_g=1$, two bandgaps are observed, with central frequencies of $f_c \approx 0.445\times10^{15}$ Hz and $f_c \approx 0.632\times10^{15}$ Hz. (Though these are not clear in Fig. 4, due to the complex form of the TE and TM combined band structure, they are clearly evident in Fig. 3.) The bandgap with the lower central frequency is caused by the crossing of the unscattered TE_1 guided mode and the Bragg-scattered TE_1 guided mode (scattering from $+k_g$). The bandgap at the higher central frequency is formed by the crossing of the unscattered TE_2 mode and the Bragg-scattered TE_2 guided mode (scattering from $+k_g$). This bandgap formation at the first BZ boundary is well known, being caused by the formation of two standing waves. To understand the physics of the bandgaps, it is helpful to investigate the time-averaged field distributions for the coupled guided modes. Since there are no E_x and E_y (x, y, and z axes defined in Fig. 1) components of the electric field for TE polarization incident at $\varphi=0°$, we plot the E_z profiles at the resonant frequencies of 0.6545×10^{15} and 0.6125×10^{15} Hz at polar angles $\theta=38.2°$ and 41.6° in Figs. 5(a) and 5(b), respectively. Clearly we see from Fig. 3(a) that the two modes considered here belong to the upper and lower branch of the bandgap ($f_c \approx 0.632\times10^{15}$ Hz), respectively. Relative to the corrugation, the field maxima in Fig. 5(a) are observed to align with the peaks of the grating, in contrast with Fig. 5(b), in which the maxima are observed to align with the troughs. In addition to these bandgaps at the zone boundary, an anticrossing between the Bragg-scattered TE_1 mode (scattering from $+k_g$) and the unscattered TE_2 guided mode arises in the visible range within the BZ ($2k_{//}/k_g \approx 0.6$).

Figure 3(d) shows the TM reflectivity for an azimuth angle of $\varphi=90°$. By comparison with the band structure shown in Fig. 4, the two modes that can be accessed in the visible range are identified as the TM_1 and TM_2 guided modes. Similarly, Fig. 3(c) shows the TE reflectivity for an

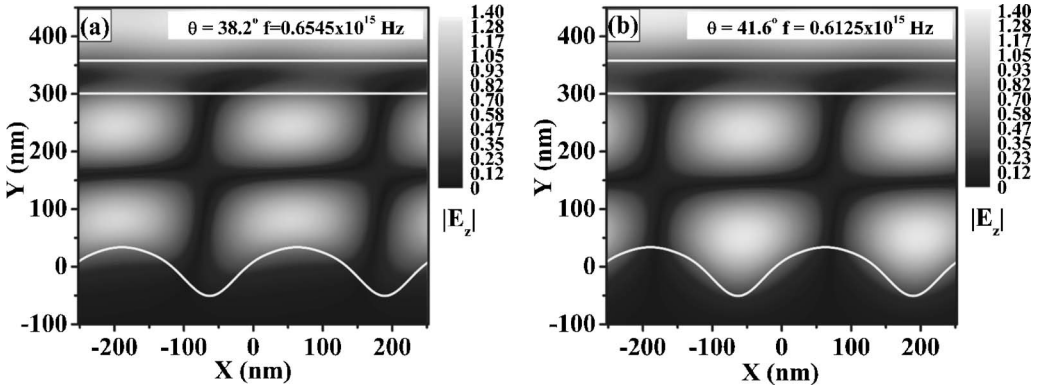

Fig. 5. Time-averaged E_z profiles for TE polarization $\varphi=0°$ at (a) $f=0.6545\times10^{15}$ Hz and $\theta=38.2°$, (b) $f=0.6125\times10^{15}$ Hz and $\theta=41.6°$. The top white solid line represents the silica/silver interface; the middle one represents the silver/resist plane interface and the bottom, corrugated, curve represents the silver/resist interface.

azimuth angle of $\varphi=90°$, with the two lowest modes in the visible range being identified as the TE_1 and TE_2 guided modes, respectively. A feature of note is that the TE_1 and TE_2 guided modes at $\varphi=90°$ are redshifted compared to the TE_1 and TE_2 guided modes at $\varphi=0°$ shown in Fig. 3(a). This frequency shift arises due to the different effective mean thickness of the waveguide medium that is sensed by incident radiation with different electric field directions relative to the grating, as noted by others (see, e.g., Watts *et al.* [23]). To understand this frequency redshift, the electric field profiles are investigated. Figures 6(a) and 6(b) show the time-averaged E_x and E_z profiles at normal incidence for the TE_2 guided mode with a resonant frequency of 0.514×10^{15} Hz at $\varphi=90°$ and $\varphi=0°$ in a planar microcavity structure, in which the thickness of the upper silver layer and resist waveguide medium are 56.8 and 300.8 nm, respectively. For TE polarization at $\varphi=90°$ and $\varphi=0°$ there can be no difference, and thus the E_x profile at $\varphi=90°$ and E_z profile at $\varphi=0°$ are identical. By contrast, in a corrugated microcavity the E_x field distribution for the TE_2 guided mode at $\varphi=90°$ and the E_z field distribution at $\varphi=0°$, plotted in Figs. 6(c) and 6(d), show a marked difference. For TE at $\varphi=0°$ the incident electric field is parallel to the grating grooves while at $\varphi=90°$ it is parallel to the grating vector. It is apparent that the locations of field maxima and minima in the y direction in Figs. 6(b) and 6(d), in which the electric field is parallel to the grating grooves, are almost identical. This is because incident radiation polarized accordingly will penetrate the grooves of the corrugation, reflecting directly from the grating surface and giving a reflection as if from a flat interface at the mean surface position. Thus the field maxima and minima will be almost unchanged from an equivalent planar system, resulting in an unchanged resonant frequency. However, when the electric field is normal to the grating grooves, a circulating field may be set up in the grooves, as shown in Fig. 6(c), which leads to an increase in effective mean thickness of the guiding medium (evidenced by the change in y position of the field node). Therefore, in the microcavity structure with corrugations, for a given in-plane wave vector, the TE_m guided mode excited at $\varphi=90°$ is always situated at a lower frequency than the same order TE_m guided mode at $\varphi=0°$. A similar analysis can be applied to the TM guided modes except that, due to the switch of the electric field orientation with azimuthal angle when compared to TE polarized light, the TM_m guided modes at $\varphi=0°$ will now occur redshifted relative to the TM_m guided modes at $\varphi=90°$. This is clearly evident in Figs. 3(b) and 3(d). Also note that SPP modes can be accessed by TE polarization at $\varphi=90°$. By comparison with the band structure in Fig. 4, the highest frequency mode in the visible range in Fig. 3(c) is identified as the SPP mode that is supported at the resist/silver interface.

At an azimuthal angle of $\varphi=0°$, the TM polarized dispersion curve becomes more complicated, as shown in Fig. 3(b). The major reason is that grating coupling allows the SPP modes supported at both the resist/silver and silver/silica interfaces to be excited. Consequently, in addition to the crossings between the TM guided modes, the scat-

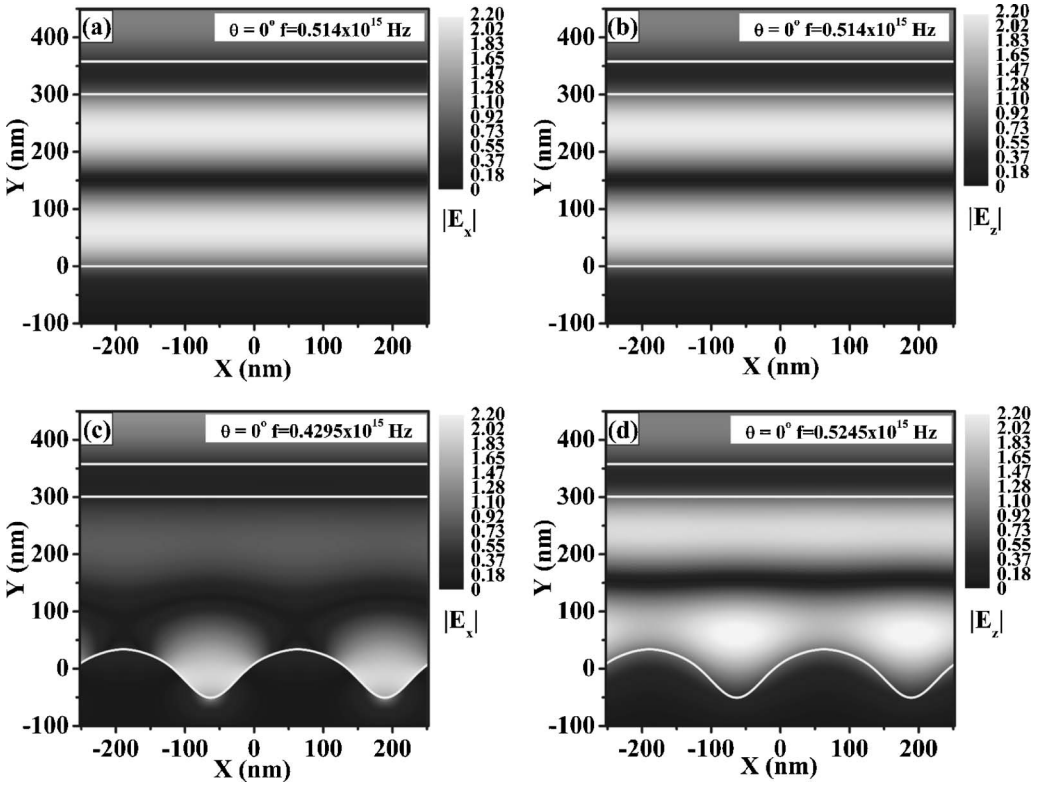

Fig. 6. Time-averaged E_x and E_z profiles for TE_2 guided modes at $\theta=0°$. (a) E_x profile in the planar structure at $f=0.514\times10^{15}$ Hz, $\varphi=90°$, (b) E_z profile in the planar structure at $f=0.514\times10^{15}$ Hz, $\varphi=0°$, (c) E_x profile in the microcavity structure with corrugations at $f=0.4295\times10^{15}$ Hz, $\varphi=90°$, and (d) E_z profile in the microcavity structure with corrugations at $f=0.5245\times10^{15}$ Hz, $\varphi=0°$. The thickness of the upper silver layer and resist waveguide medium are 56.8 and 300.8 nm, respectively, for the planar structure.

tered SPP modes may also interfere with the TM guided modes. To clearly demonstrate how the corrugation modifies the dispersion curves we have investigated the microcavity for corrugations of different amplitude. In Figs. 7(a)–7(d), the band structure associated with the microcavity at $\varphi=0°$, for amplitudes of corrugation of 5, 15, 30, and 40 nm, respectively, are plotted. For these calculations, the corrugation is purely sinusoidal, the thickness of the upper silver layer is 56.8 nm, and the mean thickness of the waveguide resist medium is 300.8 nm. The TM modes in Fig. 7(a) can be identified as being (i) the unscattered SPP at the silver/resist interface, (ii) the unscattered SPP at the silver/silica interface, (iii) the unscattered TM_1 guided mode, (iv) the unscattered TM_2 guided mode, (v) the Bragg-scattered SPP at the silver/resist interface, coupled via a Bragg-scatter of $+k_g$, (vi) the Bragg-scattered TM_1 guided mode, coupled via a Bragg-scatter of $+k_g$, (vii) the Bragg-scattered SPP at the silver/silica interface, coupled via a Bragg-scatter of $+k_g$, and (viii) the Bragg-scattered TM_2 guided mode, coupled via a Bragg-scatter of $+k_g$. Figure 7(a) clearly shows that at points where the modes cross each other bandgaps and anticrossings may be observed. We have discussed the reason for the formation of bandgaps and anticrossings in the case of TE polarization at $\varphi=0°$. Here, we concentrate on the anticrossing caused by the unscattered TM_2 guided mode (mode iv) interfering with both the scattered TM_1 mode (mode vi) and the scattered SPP mode (mode v). This area is indicated by the dashed line boxes in Fig. 7. The resonant frequency at normal incidence of the flat-band clearly reduces as the grating amplitude is increased. This is partly because the effective mean thickness of the guiding medium increases, as mentioned previously, such that the TM_2 guided mode will be red-shifted with increasing amplitude. The intermode coupling, which causes the clear anticrossing behavior between the TM_2 guided mode and both the silver/resist SPP mode and the TM_1 guided mode present at small amplitudes, becomes stronger, leading to larger anticrossing gaps. These strong anticrossings explain the large difference between the observed dispersion of the mode on these corrugated samples with that observed for planar samples. The reduction of the excitation frequency of the TM_2 guided mode coupled with the anticrossing leads to the very flat dispersion of the TM_2 guided mode, which is situated at approximately 0.43×10^{15} Hz. This is also confirmed by our experiments as shown in Fig. 3(b). By investigating the fields at near normal incidence for this resonance, shown in Fig. 8, the mixed TM_2 guided mode/SPP character of the mode is clearly evident, confirming

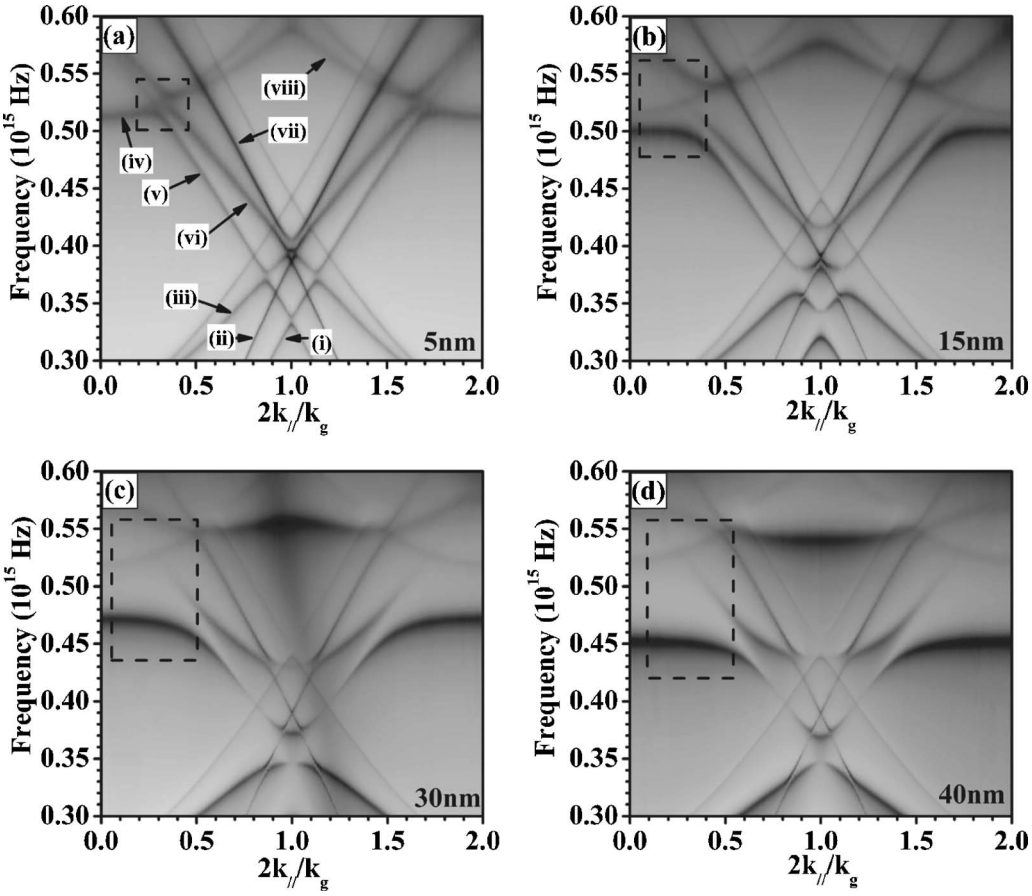

Fig. 7. Theoretical band predictions for the waveguide structure at $\varphi=0°$, with a sinusoidal grating of amplitude (a) 5, (b) 15, (c) 30, and (d) 40 nm. The modes in (a) can be identified as (i) unscattered SPP at the silver/resist interface, (ii) unscattered SPP at the silver/silica interface, (iii) unscattered TM_1 guided mode, (iv) unscattered TM_2 guided mode, (v) scattered SPP at the silver/resist interface ($+k_g$), (vi) scattered TM_1 guided mode ($+k_g$), (vii) scattered SPP at the silver/silica interface ($+k_g$), and (viii) scattered TM_2 guided mode ($+k_g$). The dashed line box in each plot indicates the anticrossing caused by the mode iv (unscattered TM_2 guided mode) interfering with both the mode vi (scattered TM_1 mode) and mode v (scattered SPP mode).

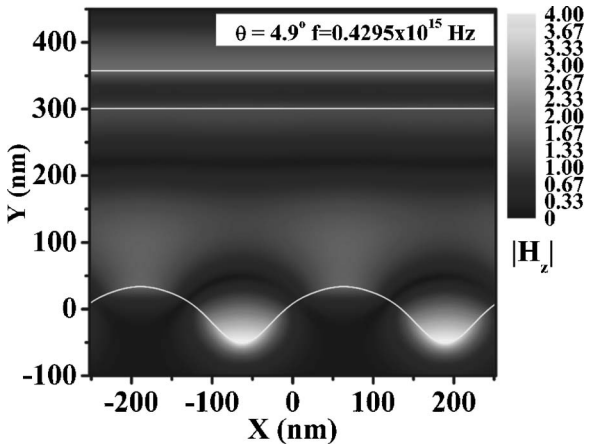

Fig. 8. Time-averaged H_z profile for the mode at $\varphi=0°$ with a resonant frequency $f=0.4295\times10^{15}$ Hz and polar angle $\theta=4.9°$.

the influence of the anticrossing on the formation of the flat band.

3. CONCLUSIONS

The visible electromagnetic response of a metal–dielectric–metal structure in which the upper interface between the dielectric and the metal is periodically corrugated has been explored at azimuth angles of $\varphi=0°$ and 90°. Reflection spectra ($410\leq\lambda_0\leq850$ nm) at both φ for 20 different polar angles ($4.9°\leq\theta\leq65.0°$) and for both TM and TE polarization have been measured and mapped onto a plot of reflectivity as a function of frequency and in-plane wave vector. The photonic bandgaps at the Brillouin zone boundary and anticrossings within the Brillouin zone are observed directly in the experimental dispersion curves. The presence of a flat photonic band caused by the anticrossings between surface plasmon polaritons and waveguide modes is confirmed experimentally. It is worth noting that the resonant frequency of this flat photonic band can be designed through appropriate choice of thickness of the guide medium and the amplitude of the grating. To understand the nature of these results, the optical field distribution at the resonant frequency is explored.

In the context of emissive devices both the bandgaps at the BZ boundary and the anticrossings within the BZ can play important roles in controlling the emission from such waveguide structures. In particular, the flat photonic bands are important for all-angle efficient enhancement in light-emitting diodes and photodetectors.

ACKNOWLEDGMENTS

Z. Chen acknowledges the financial support of an Overseas Research Studentship and from the University of Exeter.

REFERENCES AND NOTES

1. E. F. Schubert, N. E. J. Hunt, M. Micovic, R. J. Malik, D. L. Sivco, A. Y. Cho, and G. J. Zydzik, "Highly efficient light-emitting diodes with microcavities," Science **265**, 943–945 (1994).
2. L. H. Smith, J. A. E. Wasey, and W. L. Barnes, "Light outcoupling efficiency of top-emitting organic light-emitting diodes," Appl. Phys. Lett. **84**, 2986–2988 (2004).
3. C. L. Lin, H. W. Lin, and C. C. Wu, "Examining microcavity organic light-emitting devices having two metal mirrors," Appl. Phys. Lett. **87**, 0211011 (2005).
4. A. Chin and T. Y. Chang, "Enhancement of quantum efficiency in thin photodiodes through absorptive resonance," J. Lightwave Technol. **9**, 321–328 (1991).
5. R. J. Simes, R. H. Yan, R. S. Geels, L. A. Coldren, J. H. English, A. C. Gossard, and D. G. Lishan, "Electrically tunable Fabry–Perot mirror using multiple quantum well index modulation," Appl. Phys. Lett. **53**, 637–639 (1988).
6. H. Shin, M. F. Yanik, S. Fan, R. Zia, and M. L. Brongersma, "Omnidirectional resonance in a metal-dielectric-metal geometry," Appl. Phys. Lett. **84**, 4421–4423 (2004).
7. A. Hosseini and Y. Massoud, "Optical range microcavities and filters using multiple dielectric layers in metal-insulator-metal structures," J. Opt. Soc. Am. A **24**, 221–224 (2007).
8. M. Lipson and L. C. Kimerling, "Er^{3+} in strong light-confining microcavity," Appl. Phys. Lett. **77**, 1150–1152 (2000).
9. H. Raether, *Surface Plasmons* (Springer-Verlag, 1988).
10. P. K. Tien, "Integrated optics and new wave phenomena in optical waveguides," Rev. Mod. Phys. **49**, 361–420 (1977).
11. J. M. Lupton, B. J. Matterson, I. D. W. Samuel, M. J. Jory, and W. L. Barnes, "Bragg scattering from periodically microstructured light emitting diodes," Appl. Phys. Lett. **77**, 3340–3342 (2000).
12. R. K. Lee, O. J. Painter, B. D'Urso, A. Scherer, and A. Yariv, "Measurement of spontaneous emission from a two-dimensional photonic band gap defined microcavity at near-infrared wavelengths," Appl. Phys. Lett. **74**, 1522–1524 (1999).
13. M. G. Salt and W. L. Barnes, "Photonic band gaps in guided modes of textured metallic microcavities," Opt. Commun. **166**, 151–162 (1999).
14. I. Abram and G. Bourdon, "Photonic-well microcavities for spontaneous emission control," Phys. Rev. A **54**, 3476–3479 (1996).
15. W. L. Barnes, "Electromagnetic crystals for surface plasmon polaritons and the extraction of light from emissive devices," J. Lightwave Technol. **17**, 2170–2182 (1999).
16. J. P. Dowling, M. Scalora, M. J. Bloemer, and C. M. Bowden, "The photonic band-edge laser–a new approach to gain enhancement," J. Appl. Phys. **75**, 1896–1899 (1994).
17. S. C. Kitson, W. L. Barnes, and J. R. Sambles, "Photonic band gaps in metallic microcavities," J. Appl. Phys. **84**, 2399–2403 (1998).
18. M. G. Salt and W. L. Barnes, "Flat photonic bands in guided modes of textured metallic microcavities," Phys. Rev. B **61**, 11125–11135 (2000).
19. J. Chandezon, M. T. Dupuis, G. Cornet, and D. Maystre, "Multicoated gratings—a differential formalism applicable in the entire optical region," J. Opt. Soc. Am. **72**, 839–846 (1982).
20. E. L. Wood, J. R. Sambles, N. P. Cotter, and S. C. Kitson, "Diffraction grating characterization using multiple-wavelength excitation of surface-plasmon polaritons," J. Mod. Opt. **42**, 1343–1349 (1995).
21. R. A. Watts, T. W. Preist, and J. R. Sambles, "Sharp surface-plasmon resonances on deep diffraction gratings," Phys. Rev. Lett. **79**, 3978–3981 (1997).
22. $\varepsilon_{\text{silver}}(\omega)=-255.3185+198.63\omega-60.794\omega^2+8.381\omega^3-0.43004\omega^4+i(82.2575-132.79\omega+90.474\omega^2-32.88\omega^3+6.659\omega^4-0.70893\omega^5+0.030913\omega^6)$, and $\varepsilon_{\text{resist}}(\omega)=-2.35348+5.7749\omega-2.5344\omega^2+0.53253\omega^3-0.052274\omega^4+0.0018284\omega^5+i(0.01319-8.7131\times10^{-16}\omega-1.1024\times10^{-3}\omega^2-1.6659\times10^{-24}\omega^3+9.663\times10^{-5}\omega^4-1.4567\times10^{-18}\omega^5)$, where $\omega=(2\pi c/\lambda)\times10^{-15}\,\text{s}^{-1}$.
23. R. A. Watts and J. R. Sambles, "Reflection gratings as polarization converters," Opt. Commun. **140**, 179–183 (1997).